Resonant penetrative convection with an internal heat source/sink

B. Straughan*
Department of Mathematics
University of Durham, DH1 3LE, U.K.

December 3, 2018

Abstract

We develop a detailed linear instability and nonlinear stability analysis for the situation of convection in a horizontal plane layer of fluid when there is a heat sink / source which is linear in the vertical coordinate which is in the opposite direction to gravity. This can give rise to a scenario where the layer effectively splits into three sublayers. In the lowest one the fluid has a tendency to be convectively unstable while in the intermediate layer it will be gravitationally stable. In the top layer there is again the possibility for the layer to be unstable. This results in a problem where convection may initiate in either the lowest layer, the upmost layer, or perhaps in both sublayers simultaneously. In the last case there is the possibility of resonance between the upmost and lowest layers. In all cases penetrative convection may occur where convective movement in one layer induces motion in an adjacent sublayer. In certain cases the critical Rayleigh number for thermal convection may display a very rapid increase which is much greater than normal. Such behaviour may have application in energy research such as in thermal insulation.

1 Introduction

Thermal convection in a plane layer in the presence of an internal heat source or sink is a well studied phenomenon. In particular, the presence of a heat source or sink may give rise to the idea of penetrative convection where part of the layer has a tendency to move whereas the remainder of the layer will remain motionless until a certain point when movement in the rest of the layer "penetrates" into the stable layer and a resultant motion then ensues, cf. Altawallbeh *et al.* [1], van den Berg *et al.* [3], Berlengiero *et al.* [4], Capone *et al.* [5, 6, 7], Capone

*Research supported by a "Tipping Points, Mathematics, Metaphors and Meanings" grant of the Leverhulme Trust. I should like to thank an anonymous referee for pointing out some errors and for several helpful remarks.

& de Luca [8], Capone *et al.* [9], Capone & Rionero [10], Carr [11], Chasnov & Tse [13], Hetsroni *et al.* [19], Hill [20, 21], Imamura *et al.* [23], Kirillov *et al.* [26], Krishnamurti [27], Kuznetsova & Sibgatullin [28], Larson [29, 30], Machado *et al.* [32], Mharzi *et al.* [33], Papanicolaou *et al.* [36], Prudhomme & Jasmin [37], Saravan & Nayaki [47], Shalbaf *et al.* [49], Siddheshwar & Titus [51], Storesletten & Titus [52], Straughan [53, 55, 54, 60, 62], and Straughan & Walker [64]. Straughan [54], section 17.2, pp. 316–318, shows that the penetrative convection model with an internal heat sink is mathematically equivalent to the adjoint of the model with no heat sink but with a quadratic dependence on temperature in the buoyancy force in the momentum equation. However, the mathematical equations are in some ways simpler since no nonlinearities arise due to the nonlinear density in the buoyancy force.

The subject of penetrative convection is one with immense application. For example, Straughan [54], chapter 17, discusses applications in geophysics, Krishnamurti [27], Larson [29, 30] and Berlengiero *et al.* [4] analyse applications in atmospheric physics, Mharzi *et al.* [33] consider applications in building design, Tikhomolov [65] shows penetrative convection occurs in the Sun, Kaminski *et al.* [25] show that penetrative convection may be responsible for assisting the rise of volcanic plumes into the Earth's atmosphere, Kirillov *et al.* [26] discuss penetrative convection in the Laptev Sea coastal pycnocline layer, van den Berg *et al.* [3] investigate the deep mantle of exosolar planets while Imamura *et al.* [23] analyse penetration in clouds surrounding Venus, Machado *et al.* [32] analyse penetrative convective clouds in connection with cloud to ground electrical discharges, and Prudhomme & Jasmin [37] study internal heat source convection when the heat source occurs in a porous biological material due to organic decay involving microbial activity.

Resonance in thermal convection likewise has many applications since interactions between the fluid layers may greatly increase the critical Rayleigh number threshold for the onset of convection, which in turn is of interest to the energy industry. In particular, with modern heat transfer devices being increasingly employed on a micro - scale there is much need to understand penetrative and resonant convection on a nanoscale, cf. Asadzadeh *et al.* [2], Duan [15], Fan & Wang [18], Murshed *et al.* [34], Narasimhan & Reddy [35] Shojaeian & Shojaeian [50], Straughan [58, 59, 62, 63]. MEMS (micro - electro - mechanical - systems) will play an important part in future heat transfer technology, cf. Shojaeian & Shojaeian [50], therefore, we believe our analysis of thermal convection influenced by a heat sink / source is justified.

The goal of this paper is to develop a model for penetrative convection involving a heat source which varies linearly with vertical height across the layer. This allows us to obtain very strong resonance between sub-layers. The mathematical analysis involves a linear instability technique which yields a definite instability boundary coupled with a global nonlinear energy stability analysis which yields a definite stability threshold. It is worth pointing out that such analyses for a constant heat source have been performed previously, cf. Joseph & Shir [24], Roberts [43], Rionero & Straughan [42], although the richness of the results for resonance obtained here are not found with a constant heat source

or sink. Rionero & Straughan [42] did allow both gravity and the heat source to depend on the vertical coordinate, but they did not investigate resonance.

2 Basic equations

Consider an incompressible fluid contained between the planes $z = 0$ and $z = d$. The energy balance equation for such a fluid has form

$$\frac{\partial T}{\partial t} + v_i \frac{\partial T}{\partial x_i} = \kappa \Delta T + Q(z), \tag{1}$$

where T and $\mathbf{v}$ are the temperature and the velocity at a point $\mathbf{x}$ at time t. Standard indicial notation is used throughout with Δ denoting the Laplacian, κ is the thermal diffusivity, and $Q(z)$ is the heat source or sink. We here take

$$Q(z) = \tilde{Q}_0 + \tilde{Q}_1 z \tag{2}$$

for constants $\tilde{Q}_0, \tilde{Q}_1$. Equation (1) holds in the domain $\{(x, y) \in \mathbb{R}^2\} \times \{z \in (0, d)\}$ for $t > 0$.

To complete the system of equations we have the balance of mass equation

$$\frac{\partial v_i}{\partial x_i} = 0, \tag{3}$$

and the momentum equation

$$\rho_0 \Big(\frac{\partial v_i}{\partial t} + v_j \frac{\partial v_i}{\partial x_j} \Big) = -\frac{\partial p}{\partial x_i} + \mu \Delta v_i - g k_i \, \rho(T) \, , \tag{4}$$

where $\rho(T)$ is linear in temperature, and has form

$$\rho(T) = \rho_0 (1 - \alpha [T - T_0]). \tag{5}$$

In equation (5) α is the coefficient of thermal expansion and in deriving (4) we have employed a Boussinesq approximation, cf. Straughan [54], pp. 47–49. The constant ρ_0 is the density of the fluid at temperature T_0, g is gravity, μ is the dynamic viscosity, and $\mathbf{k} = (0, 0, 1)$.

We seek a motionless steady solution of form

$$\bar{v}_i \equiv 0, \qquad \bar{T} = \bar{T}(z), \qquad \bar{p} = \bar{p}(z).$$

From equation (1) we thus have to solve the ordinary differential equation

$$\bar{T}'' = -Q_0 - Q_1 z \tag{6}$$

where $Q_0 = \tilde{Q}_0/\kappa$ and $Q_1 = \tilde{Q}_1/\kappa$. We impose a heat function Q such that $\bar{T}$ has the profile shown in figure 1.

The temperature is kept constant on the boundaries $z = 0, d$, with $\bar{T} = T_L$ at $z = 0$, and $\bar{T} = T_U$ at $z = d$, $T_L > T_U$.

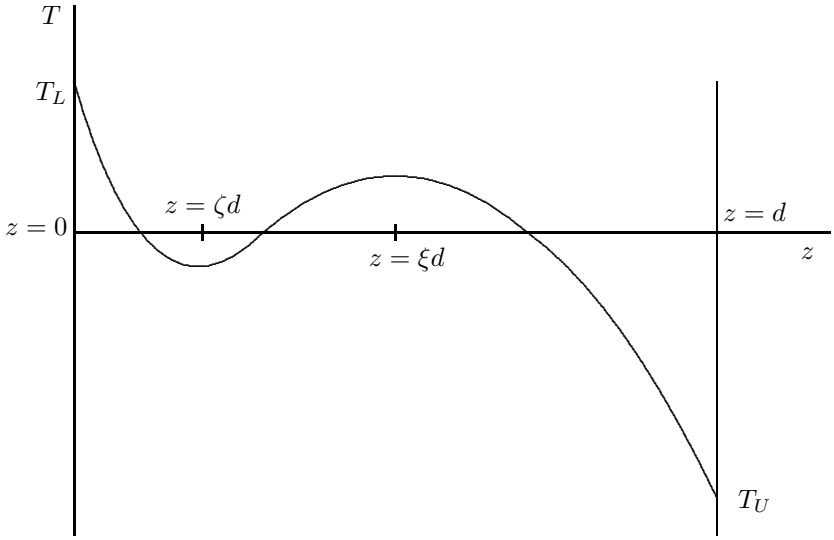

Figure 1: Steady state temperature profile

In this situation there is a possibility of convective instability driven by the sublayer $(0, \zeta d)$ or by $(\xi d, d)$ where $z = \zeta d$ and $z = \xi d$ are turning points for $\bar{T}(z)$. The solution to (6) which satisfies the boundary conditions is

$$\bar{T}(z) = -\frac{Q_0}{2}\, z^2 - \frac{Q_1}{6}\, z^3 + \Big(\frac{Q_0 d}{2} + \frac{Q_1 d^2}{6} - \beta\Big)\, z + T_L\,, \tag{7}$$

where β is the temperature gradient given by

$$\beta = \frac{T_L - T_U}{d} \;>\; 0.$$

The derivative $\bar{T}'$ is then given by

$$\bar{T}'(z) = -Q_1 d^2 \left[\frac{Q_0}{Q_1 d}\Big(\frac{z}{d} - \frac{1}{2}\Big) + \frac{1}{2}\Big(\frac{z^2}{d^2} - \frac{1}{3}\Big)\right] - \beta\,. \tag{8}$$

The turning points for $\bar{T}$ are found from (8) as

$$z = -\frac{Q_0}{Q_1} \pm \frac{1}{Q_1}\sqrt{Q_0^2 - 2Q_1\left(\beta - \frac{Q_0 d}{2} - \frac{Q_1 d^2}{6}\right)}\,. \tag{9}$$

To achieve the profile of figure 1 we require $Q_1 > 0$, $Q_0 < 0$.

The momentum equation reduces to

$$\frac{\partial \bar{p}}{\partial z} = g\rho_0\big[\alpha(\bar{T} - T_0) - 1\big]$$

and this yields the steady pressure $\bar{p}(z)$, up to a constant selected opportunely.

To study stability of the steady solution $(\bar{v}_i, \bar{T}, \bar{p})$ we let (u_i, θ, π) be perturbations so that $v_i = \bar{v}_i + u_i$, $T = \bar{T} + \theta$ and $p = \bar{p} + \pi$. We derive equations for (u_i, θ, π) and then non-dimensionalize with length, time and velocity scales as $d, d^2/\nu, \nu/d$, where $\nu = \mu/\rho_0$ is the kinematic viscosity. Then with temperature scale $T^\sharp = Ud\sqrt{Q_1\nu/\kappa\alpha g}$, pressure scale $P = \nu U \rho_0/d$, we put

$$A_1 = \Big|\frac{Q_0}{Q_1 d}\Big|, \qquad B = \frac{\beta}{Q_1 d^2}$$

and define the Prandtl and Rayleigh numbers, Pr and Ra by

$$Pr = \frac{\nu}{\kappa}\,, \qquad Ra = \frac{d^6 Q_1 \alpha g}{\kappa\nu}\,. \tag{10}$$

With these scalings the non-dimensional perturbation equations are found to be

$$\begin{aligned} &u_{i,t} + u_j u_{i,j} = -\pi_{,i} + R\theta k_i + \Delta u_i, \\ &u_{i,i} = 0, \\ &Pr(\theta_{,t} + u_i\theta_{,i}) = \Delta\theta + RF(z)w, \end{aligned} \tag{11}$$

where $R = \sqrt{Ra}$, $u_3 = w$, and where F is minus the non-dimensional temperature gradient given by

$$F(z) = -A_1\Big(z - \frac{1}{2}\Big) + \frac{1}{2}\Big(z^2 - \frac{1}{3}\Big) + B,$$

equations (11) holding on the domain $\mathbb{R}^2 \times \{z \in (0,1)\} \times \{t > 0\}$. On the boundaries we have

$$u_i = 0, \quad \theta = 0, \qquad z = 0, 1, \tag{12}$$

and (u_i, θ, π) satisfy a plane tiling periodic form in the (x, y) directions.

From equation (9) one may show

$$\begin{pmatrix}\xi\\ \zeta\end{pmatrix} = A_1 \pm \sqrt{A_1^2 - 2B - A_1 + \frac{1}{3}}\,, \tag{13}$$

and also

$$A_1 = \frac{\xi + \zeta}{2}\,, \qquad B = \frac{\xi\zeta}{2} - \Big(\frac{\xi + \zeta}{4}\Big) + \frac{1}{6}\,. \tag{14}$$

It is worth noting that if $\xi + \zeta = 1$ then $B = \xi(1-\xi)/2 - 1/12$ and then the fact that B must be positive yields the restriction on ξ,

$$0.211325 \approx \frac{1}{2} - \frac{1}{\sqrt{12}} < \xi < \frac{1}{2} + \frac{1}{\sqrt{12}} \approx 0.788675. \tag{15}$$

These conditions ensure $B > 0$ and we cannot have ξ out of this range.

We may define different Rayleigh numbers Ra_1 and Ra_2 in terms of the depths $d_1 = \zeta$ and $d_2 = 1 - \xi$ and since $Ra \propto d^6$ this suggests resonance may occur with $d_1 = d_2$, i.e. $Ra_1 = Ra_2$ when $d_1^6 = d_2^6$, so when $d_1 = d_2$. This is investigated in detail in section 5. For some purposes it may be useful to introduce the alternative Rayleigh numbers, Ra_C, the classical one, and Ra_0, based on Q_0 rather than Q_1, defined by

$$Ra_C = \frac{\alpha g \beta d^4}{\kappa\nu} \qquad \text{and} \qquad Ra_0 = \frac{\alpha g d^5 |Q_0|}{\kappa\nu}\,. \tag{16}$$

One may then check that these numbers are related to Ra by the formulae

$$Ra_0 = A_1 Ra \qquad \text{and} \qquad Ra_C = Ra\Big(\frac{\xi\zeta}{2} - \frac{\xi + \zeta}{4} + \frac{1}{6}\Big)\,.$$

3 Linear instability

To investigate linear instability we linearize equations (11) and then seek solutions like $u_i = e^{\sigma t} u_i(\mathbf{x})$, $\theta = e^{\sigma t}\theta(\mathbf{x})$, $\pi = e^{\sigma t}\pi(\mathbf{x})$. Then removing the pressure π we may reduce the linearized system to

$$\begin{aligned} \sigma\Delta w &= \Delta^2 w + R\Delta^* \theta,\\ \sigma Pr\,\theta &= RFw + \Delta\theta, \end{aligned} \tag{17}$$

where $\Delta^* = \partial^2/\partial x^2 + \partial^2/\partial y^2$, and (17) hold on $\mathbb{R}^2 \times (0,1)$. We now put $w = W(z)f(x,y)$, $\theta = \Theta(z)f(x,y)$, where f is a planform function which tiles the plane and satisfies

$$\Delta^* f = -a^2 f \tag{18}$$

for a wavenumber a. Such planforms are discussed in e.g. Chandrasekhar [12], pp. 43–52, and Straughan [54], p. 51.

The above procedure results in having to solve the eigenvalue system

$$\begin{aligned} &(D^2 - a^2)^2 W - Ra^2\Theta = \sigma(D^2 - a^2)W \\ &(D^2 - a^2)\Theta + RFW = \sigma Pr\Theta, \end{aligned} \tag{19}$$

where $D = d/dz$ and $z \in (0,1)$. The boundary conditions for two fixed surfaces are

$$W = DW = \Theta = 0, \qquad z = 0, 1. \tag{20}$$

System (19) together with the boundary conditions (20) is solved numerically by the D^2-Chebyshev tau method, cf. Dongarra *et al.* [14], and numerical output is included in section 5.

Remarks.

1. If we consider equations (17), or (19), but replace the boundary conditions (20) by those for two stress free surfaces then one can demonstrate that exchange of stabilities holds. By this we mean that if $\sigma = \sigma_r + i\sigma_i$, then one can show $\sigma_i \neq 0 \implies \sigma_r < 0$, cf. Straughan [54]. Thus, in that case oscillatory convection cannot occur. Even for the fixed surface case considered here we still find numerically that instability is by stationary convection.
2. Instead of employing a heat source / sink we can put $Q \equiv 0$ and replace $\rho(T)$ in (5) with $\rho(T)$ a suitable cubic in T, cf. Straughan [61]. For suitable choice of cubic a similar potentially three layer system like that in figure 1 is possible. However, with this approach the perturbation equation for the momentum equation contains θ^2 and θ^3 terms which are harder to control in a nonlinear analysis. Also, from a physical point of view it is not clear one could manufacture a fluid with the precise density, whereas, in principle, a suitable heat source / sink can always be constructed.

4 Global nonlinear stability

Linearised instability theory yields a threshold for Ra such that if this is exceeded then the solution is unstable. However, it yields *nothing* about stability. One way to derive a global nonlinear stability bound (for all initial data) is to use an appropriate energy method, cf. Straughan [54]. It is worth pointing out that energy methods are increasingly employed to achieve sharp stability boundaries, cf. Capone *et al.* [5, 6, 7], Capone & De Luca [8], Capone *et al.* [9], Capone & Rionero [10], Falsaperla *et al.* [16, 17], Hill & Malashetty [22], Lombardo *et al.* [31], Rionero [38, 39, 40, 41], Saravan & Brindha [44, 45], Saravan & Sivakumar [46], Scott & Straughan [48], Straughan [54, 56, 57, 59, 62]. In this section we develop an energy stability theory for equations (11).

Let V be a period cell for the disturbance and let $\|\cdot\|$ and $(\cdot,\cdot)$ be the norm and inner product on $L^2(V)$. Next, multiply equation $(11)_1$ by u_i and integrate over V, then multiply equation $(11)_3$ by θ and integrate over V. By introducing a coupling parameter $\lambda > 0$ we may then derive

$$\frac{dE}{dt} = RI - D, \tag{21}$$

where the functions E and I are given by

$$E(t) = \frac{1}{2}\|\mathbf{u}\|^2 + \frac{\lambda Pr}{2}\|\theta\|^2, \tag{22}$$

and

$$I(t) = \Big((1+\lambda F)w, \theta\Big), \tag{23}$$

with the dissipation D being defined by

$$D(t) = \|\nabla \mathbf{u}\|^2 + \lambda\|\nabla\theta\|^2. \tag{24}$$

Define R_E by

$$\frac{1}{R_E} = \max_{\mathcal{H}} \frac{I}{D} \tag{25}$$

where $\mathcal{H}$ is the space of admissible functions, i.e. $u_i \in H^1(V)$,$\theta \in H^1(V)$, with u_i solenoidal and u_i, θ satisfying the boundary conditions. Then from (21) we derive

$$\frac{dE}{dt} \leq -D\Big(1 - \frac{R}{R_E}\Big). \tag{26}$$

Poincaré's inequality ensures that there is a constant $c > 0$ such that $D \geq cE$ and then if $R < R_E$, one may show from inequality (26) that E decays exponentially and we have global nonlinear stability, i.e. for all initial data.

The nonlinear stability threshold then requires the solution of (25). The Euler-Lagrange equations which arise from (25) are

$$\begin{aligned} &2\Delta u_i + R_E \mathcal{F}\phi k_i = -\omega_{,i}, \\ &u_{i,i} = 0, \\ &2\Delta\phi + R_E\mathcal{F}w = 0, \end{aligned} \tag{27}$$

where ω is a Lagrange multiplier, $\phi = \lambda^{1/2}\theta$, and

$$\mathcal{F} = \frac{1+\lambda F}{\sqrt{\lambda}}. \tag{28}$$

By removing the Langrange multiplier, system (27) is reduced to

$$\begin{aligned} &\Delta^2 w + R_E \frac{\mathcal{F}}{2}\Delta^*\phi = 0 \\ &\Delta\phi + R_E\frac{\mathcal{F}}{2}w = 0. \end{aligned} \tag{29}$$

Seeking a solution of form $w = W(z)f(x,y)$, $\phi = \Phi(z)f(x,y)$, we then have to solve the eigenvalue problem

$$\begin{aligned}(D^2 - a^2)^2 W - R_E \frac{\mathcal{F}}{2} a^2 \Phi = 0\,,\\ (D^2 - a^2)\Phi + R_E \frac{\mathcal{F}}{2} W = 0.\end{aligned} \tag{30}$$

System (30) is subject to the boundary conditions (20). This eigenvalue problem is solved numerically by the D^2 - Chebyshev tau method and numerical output is discussed in section 5.

5 Numerical results and conclusions

We have computed many results for the eigenvalue system (19), (20) for linear instability, and also for the system (30), (20), pertaining to nonlinear stability. We report only a fraction of the results computed, and concentrate on describing those which appear to be of most interest. Tables 1 - 3 give critical Rayleigh and wave numbers for linear instability for (ζ, ξ) in the range $(0.42, 0.58)$ to $(0.22, 0.78)$. As noted above, these are the parameter ranges we found to be of most interest. While we present many values for the combination such that $\zeta + \xi = 1$, see table 1, we also show what happens when $\zeta + \xi \neq 1$ in tables 2 and 3. Particularly noticeable is the rapid rise in Ra observed in table 3 as ζ decreases, for fixed ξ.

5.1 Eigenfunction (streamfunction) behaviour

The eigenfunctions for W corresponding to the critical values displayed in tables 1 - 3 are shown in figures 2 - 17. What we observe is that for $\zeta = 0.42, \xi = 0.58$ and for $\zeta = 0.35, \xi = 0.65$, there is no penetrative convection and the velocity reaches a maximum in the centre of the layer, see figures 2 and 3. The temperature eigenfunction behaviour is, however, different. When $\zeta = 0.42, \xi = 0.58$ the maximum temperature perturbation is achieved symmetrically and not at $z = 0.5$, and the temperature perturbation changes strongly as ξ increases, as observed with $\zeta = 0.35, \xi = 0.65$ in figure 3. The W-profile flattens out in the centre as ξ is increased with corresponding decrease in ζ as shown in figure 4, where the temperature perturbation changes even more strongly in the centre of the cell. We find that W is not a maximum at $z = 0.5$ for $\xi = 0.664$, $\zeta = 0.336$ and this behaviour is exaggerated as ξ increases, see figure 5. The temperature eigenfunction is similar to that in figure 4 excepting the change in the centre of the cell is even greater. The behaviour of W displayed in figure 5 continues when $\xi = 0.671, \zeta = 0.329$ as shown in figure 6, with the depression in W at $z = 0.5$ increasing, as is the change in the centre of the cell for Θ.

5.2 Penetrative convection

When $\xi = 0.672, \zeta = 0.328$ an abrupt change is observed and penetrative convection occurs with symmetry about $z = 0.5$, see figure 7. The temperature eigenfunction displays a similar effect with a notable convexity in the curve when $z = 0.5$. This behaviour continues with increasing ξ, see figure 8, although the temperature profile displays an even greater convexity near $z = 0.5$, nearly flattening out. As ξ increases further W still displays penetrative convection but with increasing convexity near $z = 0.5$, see figure 9, where $\zeta = 0.244, \xi = 0.756$. The temperature eigenfunction continues the strong variation near $z = 0.5$ and displays strongly changing sign, see figure 9.

5.3 Multicellular convection

Once ξ increases further, maintaining $\xi + \zeta = 1$, the W eigenfunction changes shape completely as seen in figure 10. Here penetrative convection still occurs but now with a small weak cell near $z = 0.5$ and two strong cells with opposite circulation either side of this, i.e. a three cell structure. The temperature eigenfunction likewise changes shape completely as seen in figure 10. As ξ increases maintaining $\zeta + \xi = 1$, the behaviour seen in figure 10 persists but the convection cell in the centre increases in strength, see figure 11. We cannot extend ξ much beyond this because we need to ensure the coefficient B is positive as shown earlier, (15). The temperature eigenfunction in figure 11 displays the characteristic behaviour of figure 10, but with deepening of the perturbation near $z = 0.5$.

5.4 When $\xi + \zeta \neq 1$

Figures 12 - 17 display the W eigenfunction when $\zeta + \xi \neq 1$. In particular, in figures 12, 13 we show the situation corresponding to $\zeta = 0.3, \xi = 0.7$, namely when $\zeta = 0.33, \xi = 0.7$ and $\zeta = 0.3, \xi = 0.67$. We still witness penetrative convection but with a much stronger cell in the region where ζ or $1 - \xi$ is larger. This behaviour is also observed in figures 14, 15 where $\zeta = 0.28, \xi = 0.7$ and $\zeta = 0.3, \xi = 0.72$, although the weaker cell is stronger than those in figures 12, 13. Figures 16, 17 show the W eigenfunction for $\zeta = 0.24, \xi = 0.77$, and $\zeta = 0.23, \xi = 0.76$, the case of $\zeta = 0.23, \xi = 0.77$ (not displayed here) being similar to that of figure 11 for W, although the W value at $z = 0.5$ is not so low. In figures 16, 17 we clearly see penetrative convection with a three cell structure, although one cell is much stronger than the other two.

5.5 Rapid increase of Ra

What is observed as ξ increases from 0.58 to 0.78 in table 1 and figures 2 - 11, is that Ra displays a very rapid increase from the value of $Ra = 169565$ to $Ra = 6460507$. Such a strong increase is very noticeable, and may have significant bearing on heat transfer, although one must recall the definition

of Ra given in (10) involves the heat source coefficient Q_1. One may easily calculate the equivalent values of Ra_C and Ra_0 as defined in (16), but a similar rapid increase is still witnessed. In addition, the wavenumber increases from 3.18 to 8.85 over the same ξ range. Hence, the Rayleigh number as defined in (10) increases over ten-fold whereas the wavenumber increases by over a factor of two. This means that the convection cell decreases in width for fixed height by a factor of more than one half.

5.6 Energy stability results

The nonlinear energy stability results are compared to the linear instability ones in table 4. While there is a gap between these sets of values one should realise that the nonlinear results ensure stability for all initial data. Nevertheless, sub-critical instabilities are not precluded in the region between the linear and nonlinear values.

References

[1] Altawallbeh, A. A., Bhadauria, B. S. & Hashim, I. Linear and nonlinear double - diffusive convection in a saturated anisotropic porous layer with Soret effect and internal heat source. *Int. J. Heat Mass Transfer* **59** (2013), 103–111.

[2] Asadzadeh, F., Nasr Esfahany, M. & Etesami, N. Natural convective heat transfer of Fe_3O_4 / ethylene glycol nanofluid in electric field. *Int. J. Thermal Sciences* **62** (2012), 114–119.

[3] van den Berg, A.P., Yuen, D.A., Beebe, G.L. & Christiansen, M.D. The dynamical impact of electronic thermal conductivity on deep mantle convection of exosolar planets. *Physics of the Earth and Planetary Interiors* **178** (2010), 136–154.

[4] Berlengiero, M., Emanuel, K.A., von Hardenberg, J., Provenzale, A. & Spiegel, E.A. Internally cooled convection: a fillip for Philip. *Commun. Nonlinear Sci. Numer. Simulation* **17** (2012), 1998–2007.

[5] Capone, F., Gentile, M. & Hill, A.A. Penetrative convection via internal heating in anisotropic porous media. *Mech. Research Communications* **37** (2010), 441–444.

[6] Capone, F., Gentile, M. & Hill, A.A. Penetrative convection in anisotropic porous media with variable permeability. *Acta Mechanica* **216** (2011), 49–58.

[7] Capone, F., Gentile, M. & Hill, A.A. Double diffusive penetrative convection simulated via internal heating in an anisotropic porous layer with throughflow. *Int. J. Heat Mass Transfer* **54** (2011), 1622–1626.

[8] Capone, F. & De Luca, R. Ultimately boundedness and stability of triply diffusive mixtures in rotating porous layers under the action of the Brinkman law. *Int. J. Non-Linear Mech.* **47** (2012), 799–805.

[9] Capone, F., De Cataldis, V., De Luca, R. & Torcicollo, I. On the stability of vertical constant throughflows for binary mixtures in porous layers. *Int. J. Non-Linear Mech.* **59** (2014), 1–8.

[10] Capone, F. & Rionero, S. Inertia effect on the onset of convection in rotating porous layers via the "auxilliary system method". *Int. J. Non-Linear Mech.* **57** (2013), 192–200.

[11] Carr, M. Penetrative convection in a superposed porous-medium-fluid layer via internal heating. *J. Fluid Mech.* **509** (2004), 305–329.

[12] Chandrasekhar, S. *Hydrodynamic and hydromagnetic stability*. Dover, New York (1981).

[13] Chasnov, J.R. & Tse, K.L. 2001 Turbulent penetrative convection with an internal heat source. *Fluid Dynamics Research* **28** (2001), 397-421.

[14] Dongarra, J.J., Straughan, B. & Walker, D.W. Chebyshev tau - QZ algorithm methods for calculating spectra of hydrodynamic stability problems. *Appl. Numer. Math.* **22** (1996), 399–435.

[15] Duan, Z. 2012 Second-order gaseous slip flow models in long circular and noncircular microchannels and nanochannels. *Microfluidics and Nanofluidics* **12** (2012), 805–820.

[16] Falsaperla, P., Giacobbe, A. & Mulone, G. Double diffusion in rotating porous media under general boundary conditions. *Int. J. Heat Mass Transfer* **55** (2012), 2412–2419.

[17] Falsaperla, P., Giacobbe, A. and Mulone, G. Does symmetry of the operator of a dynamical system help stability? *Acta Appl. Math.* **122** (2012), 239–253.

[18] Fan, J. & Wang, L. Review of heat conduction in nanofluids. *J. Heat Transfer* bf 133 (2011), 040801.

[19] Hetsroni, G., Gurevich, M. & Rozenblit, R. Natural convection in metal foam strips with internal heat generation. *Experimental Thermal and Fluid Science* **32** (2008), 1740–1747.

[20] Hill, A.A. Penetrative convection induced by the absorption of radiation with a nonlinear internal heat source. *Dyn. Atmospheres Oceans* **38** (2004), 57–67.

[21] Hill, A.A. 2005 Double-diffusive convection in a porous medium with a concentration based internal heat source. *Proc. Roy. Soc. London A* **461** (2005), 561–574.

[22] Hill, A.A. and Malashetty, M.S. An operative method to obtain sharp nonlinear stability for systems with spatially dependent coefficients. *Proc. Roy. Soc. London A* 468 (2012), 323–336.

[23] Imamura, T., Higuchi, T., Maejima, Y., Takagi, M., Sugimoto, N., Ikeda, K. & Ando, H. Inverse insolation dependence of Venus' cloud - level convection. *Icarus* 228 (2014), 181–188.

[24] Joseph, D.D. and Shir, C. Subcritical convective instability. Part 1. Fluid layers. *J. Fluid Mech.* 26 (1966), 753–768.

[25] Kaminski, E., Chenet, A.L., Jaupart, C. & Courtillot, V. Rise of volcanic plumes to the stratosphere aided by penetrative convection above large lava flows. *Earth Planetary Sci. Lett.* **301** (2011), 171–178.

[26] Kirillov, S.A., Dmitrenko, I.A., Hölemann, J.A., Kassens, H. & Bloshkina, E. The penetrative mixing in the Laptev sea coastal polyna pynocline layer. *Continental Shelf Research* **63** (2013), 34–42.

[27] Krishnamurti, R. Convection induced by selective absortion of radiation: A laboratory model of conditional instability. *Dynamics of Atmospheres and Oceans* **27** (1997), 367–382.

[28] Kuznetsova, D.V. & Sibgatullin, I.N. Transitional regimes of penetrative convection in a plain layer. *Doklady Physics* **56** (2011), 271–274.

[29] Larson, V.E. Stability properties of and scaling laws for a dry radiative-convective atmosphere. *Q. J. Royal Meteorological Soc.* **126** (2000), 145–171.

[30] Larson, V.E. 2001 The effects of thermal radiation on dry convective instability. *Dynamics of Atmospheres and Oceans* **34** (2001), 45–71.

[31] Lombardo, S., Mulone, G. and Trovato, M. Nonlinear stability in reaction-diffusion systems via optimal Lyapunov functions. *J. Math. Anal. Appl.* 342 (2008), 461–476.

[32] Machado, L.A.T., Lima, W.F.A., Pinto, O. & Morales, C.A. Relationship between cloud-to-ground discharge and penetrative clouds: a multi-channel satellite application. *Atmospheric Research* **93** (2009), 304–309.

[33] Mharzi, M., Daguenet, M. & Daoudi, S. Thermosolutal natural convection in a vertically layered fluid - porous medium heated from the side. *Energy Conversion and Management* **41** (2000), 1065–1090.

[34] Murshed, S.M.S., Leong, K.C. & Yang, C. Investigations of thermal conductivity and viscosity of nanofluids. *Int. J. Thermal Sciences* **47** (2008), 560–568.

[35] Narasimhan, A. & Reddy, B.V.K. 2011 Resonance of natural convection inside a bidisperse porous medium enclosure. *J. Heat Transfer - ASME* **133** (2011), 042601.

[36] Papanicolaou, N.C., Christov, C.I. & Jordan, P.M. The influence of thermal relaxation on the oscillatory properties of two-gradient convection in a vertical slot. *European J. Mech. B/Fluids* **30** (2011), 68—75.

[37] Prudh̀omme, M. & Jasmin, S. Inverse solution for a biochemical heat source in a porous medium in the presence of natural convection. *Chem. Engng. Sci.* **61** (2006), 1667—1675.

[38] Rionero, S. Onset of convection in porous materials with vertically stratfied porosity. *Acta Mechanica* **222** (2011), 261–272.

[39] Rionero, S. Absence of subcritical instabilities and global nonlinear stability for porous ternary diffusive - convective fluid mixtures. *Phys. Fluids* **24** (2012), Article Number 104101.

[40] Rionero, S. Multicomponent diffusive - convective fluid motions in porous layers: Ultimately boundedness, absence of subcritical instabilities, and global stability for any number of salts. *Phys. Fluids* **25** (2013), Article Number 054104.

[41] Rionero, S. Triple diffusive convection in porous media. *Acta Mechanica* **224** (2013), 447–458.

[42] Rionero, S. & Straughan, B. Convection in a porous medium with internal heat source and variable gravity effects. *Int. J. Engng. Sci.* **28** (1990), 497–503.

[43] Roberts, P.H. Convection in horizontal layers with internal heat generation. *J. Fluid Mech.* 30 (1967), 33–49.

[44] Saravan, S. & Brindha, D. Linear and nonlinear stability limits for centrifugal convection in an anisotropic layer. *Int. J. Non-Linear Mechanics* **46** (2011), 65–72.

[45] Saravan, S. & Brindha, D. Onset of centrifugal filtration convection: departure from thermal equilibrium. *Proc. Roy. Soc. London A* **469** (2013), 20120655.

[46] Saravan, S. & Sivakumar, T. Onset of thermovibrational filtration convection: departure from thermal equilibrium. *Phys. Rev. E* **84** (2011), 026307.

[47] Saravan, S. & Nayaki, V.P.M.S. Thermorheological effect on thermal nonequilibrium porous convection with heat generation. *Int. J. Engng. Sci.* **74** (2014), 55–64.

[48] Scott, N.L. & Straughan, B. A nonlinear stability analysis of convection in a porous vertical channel including local thermal nonequilibrium. *J. Math. Fluid Mech.*, **15** (2013), 171–178.

[49] Shalbaf, S., Noghrehabadi, A., Assari, M.R. & Dezfuli, A.D. Linear stability of natural convection in a multilayer system of fluid and porous layers with internal heat sources. *Acta Mechanica* **224** (2013), 1103–1114.

[50] Shojaeian, M. & Shojaeian, M. Analytical solution of mixed electromagnetic / pressure driven gaseous flows in microchannels. *Microfluidics and Nanofluidics* **12** (2012), 553–564.

[51] Siddheshwar, P.G. & Titus, P.S. Convection with variable heat source. *J. Heat Transfer (ASME)* **135** (2013), 122502.

[52] Storesletten, L. & Barletta, A. Linear instability of mixed convection of cold water in a porous layer induced by viscous dissipation. *Int. J. Thermal Sciences* **48** (2009), 655–664.

[53] Straughan, B. Global stability for convection induced by absorption of radiation. *Dynamics of Atmospheres and Oceans* **35** (2002), 351–361.

[54] Straughan, B. *The energy method, stability, and nonlinear convection.* Ser. Appl. Math. Sci. vol. 91, Second Edition. New York: Springer (2004).

[55] Straughan, B. Resonant porous penetrative convection. *Proc. Roy. Soc. London A*, **460** (2004), 2913–2927.

[56] Straughan, B. Global nonlinear stability in porous convection with a thermal non-equilibrium model. *Proc. Roy. Soc. London A* **462** (2006), 409–418.

[57] Straughan, B. *Stability and wave motion in porous media.* Ser. Appl. Math. Sci. vol. 165, New York: Springer (2008).

[58] Straughan, B. Green-Naghdi fluid with non-thermal equilibrium effects. *Proc. Roy. Soc. London A*, **466** (2010), 2021–2032.

[59] Straughan, B. *Heat waves.* Ser. Appl. Math. Sci. vol. 177, New York: Springer (2011).

[60] Straughan, B. Continuous dependence on the heat source in resonant porous penetrative convection. *Studies in Applied Mathematics* **127** (2011), 302–314.

[61] Straughan, B. Triply resonant penetrative convection. *Proc. Roy. Soc. London A*, **468** (2012), 3804-3823.

[62] Straughan, B. Porous convection with local thermal non-equilibrium effects and Cattaneo effects in the solid. *Proc. Roy. Soc. London A*, **469** (2013), 20130187.

[63] Straughan, B. Anisotropic inertia effect in microfluidic porous thermosolutal convection. *Microfluidics and Nanofluidics*, doi 10.1007/s10404-013-1208-7

[64] Straughan, B. & Walker, D.W. Anisotropic porous penetrative convection. *Proc. Roy. Soc. London A*, **452** (1996), 97–115.

[65] Tikhomolov, E. Large - scale vortical flows and penetrative convection in the Sun. *Nuclear Physics A* **758** (2005), 709c–712c.

ξ	ζ	Ra	a
.65	.35	585817	3.95
.67	.33	1021063	5.46
.671	.329	1043618	5.53
.672	.328	1062452	5.66
.68	.32	1151028	5.71
.69	.31	1298907	5.79
.7	.3	1468052	5.91
.71	.29	1703427	6.09
.72	.28	2014744	6.35
.73	.27	2422527	6.71
.74	.26	2943080	7.17
.75	.25	3589010	7.67
.756	.244	4043926	7.96
.758	.242	4206368	8.09
.76	.24	4360702	8.14
.77	.23	5268355	8.46
.78	.22	6460507	8.85

Table 1: Critical values of Rayleigh number and wavenumber, in linear instability theory, $\zeta + \xi = 1$.

ξ	ζ	Ra	a
.58	.38	197888	3.23
.58	.39	190480	3.21
.58	.40	183254	3.20
.58	.41	176269	3.19
.58	.42	169565	3.18
.60	.38	230552	3.24
.60	.39	217316	3.22
.60	.40	205017	3.21
.60	.41	193674	3.20
.60	.42	183255	3.20
.62	.38	273324	3.28
.62	.39	250507	3.25
.62	.40	230552	3.24
.62	.41	213130	3.23
.62	.42	197888	3.23

Table 2: Critical values of Rayleigh number and wavenumber, in linear instability theory, sum of ζ and ξ not always equal to one.

ξ	ζ	Ra	a
.76	.22	4247321	8.16
.76	.23	4307519	8.15
.76	.24	4360702	8.14
.76	.25	3575013	7.79
.76	.26	2946271	7.45
.76	.27	2444894	7.14
.77	.22	5232867	8.53
.77	.23	5268355	8.46
.77	.24	4307519	8.15
.77	.25	3525199	7.80
.77	.26	2906330	7.47
.77	.27	2412610	7.16
.78	.22	6460507	8.85
.78	.23	5232867	8.53
.78	.24	4247321	8.16
.78	.25	3476145	7.81
.78	.26	2866518	7.49
.78	.27	2380197	7.18

Table 3: Critical values of Rayleigh number and wavenumber, in linear instability theory, sum of ζ and ξ not always equal to one.

ζ	ξ	Ra_L	Ra_E	a_L	a_E	λ
.4	.6	2.05017×10^5	1.74636×10^5	3.21	3.31	85.4
.42	.6	1.83255×10^5	1.59800×10^5	3.20	3.29	79.8
.38	.6	2.30552×10^5	1.89104×10^5	3.24	3.35	88.7
.35	.65	5.85817×10^5	3.25086×10^5	3.95	3.68	110.5
.3	.7	1.468052×10^6	8.29052×10^5	5.91	4.66	95.6
.28	.7	1.520887×10^6	9.13711×10^5	6.18	4.90	83.1
.3	.72	1.520887×10^6	9.13711×10^5	6.18	4.90	83.1
.22	.78	6.460507×10^6	2.866815×10^6	8.85	4.99	40.7

Table 4: Critical values of Rayleigh number, wavenumber, and coupling parameter for linear instability and nonlinear energy stability theory.

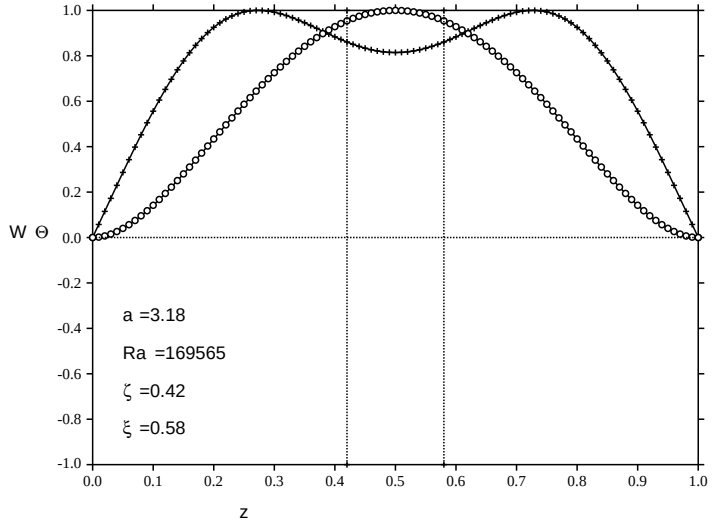

Figure 2: Linear instability eigenfunctions at criticality. The open circles represent $W(z)$ whereas the crosses are $\Theta(z)$. Parameters as on graph. The vertical dotted lines are where $\zeta = 0.42, \xi = 0.58$.

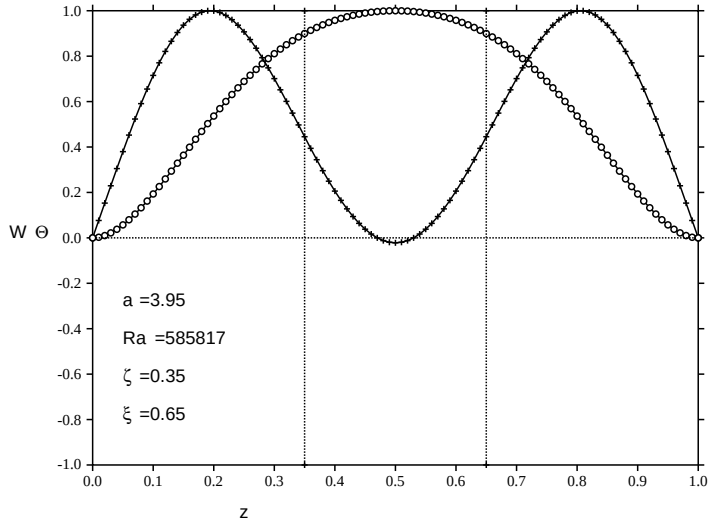

Figure 3: Linear instability eigenfunctions at criticality. The open circles represent $W(z)$ whereas the crosses are $\Theta(z)$. Parameters as on graph. The vertical dotted lines are where $\zeta = 0.35, \xi = 0.65$.

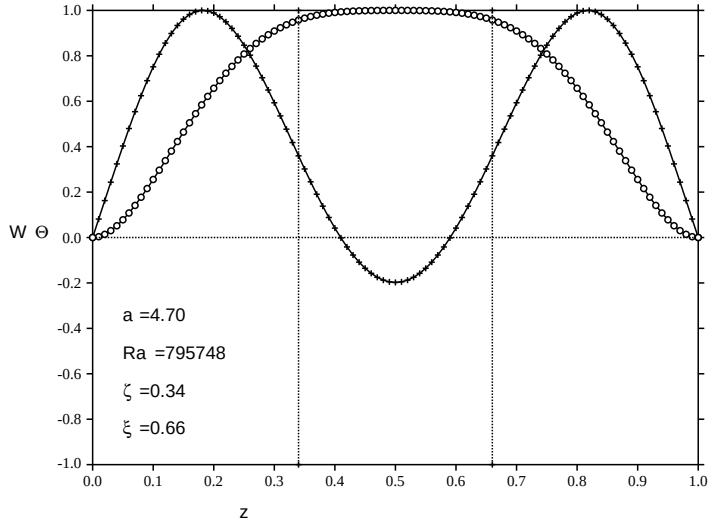

Figure 4: Linear instability eigenfunctions at criticality. The open circles represent $W(z)$ whereas the crosses are $\Theta(z)$. Parameters as on graph. The vertical dotted lines are where $\zeta = 0.34, \xi = 0.66$.

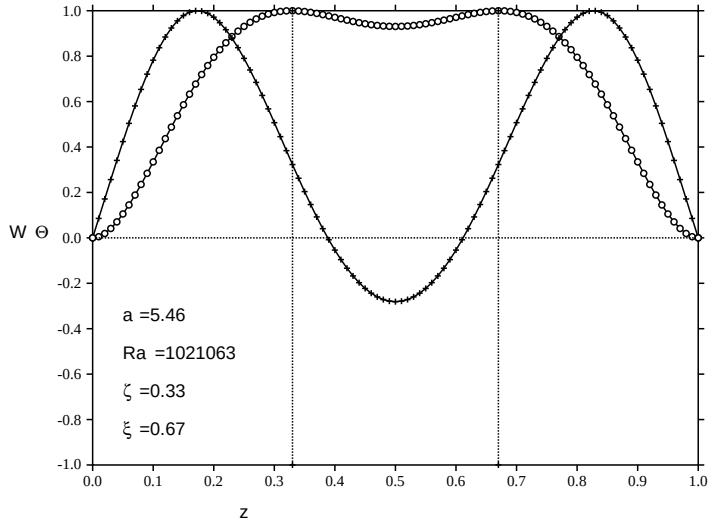

Figure 5: Linear instability eigenfunctions at criticality. The open circles represent $W(z)$ whereas the crosses are $\Theta(z)$. Parameters as on graph. The vertical dotted lines are where $\zeta = 0.33, \xi = 0.67$.

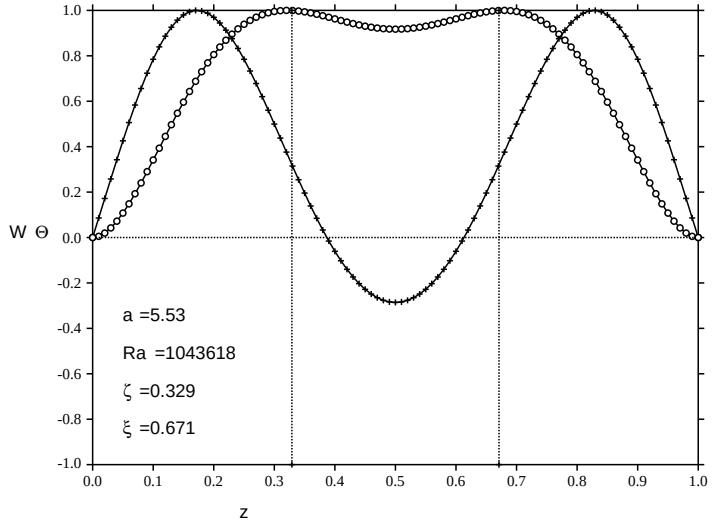

Figure 6: Linear instability eigenfunctions at criticality. The open circles represent $W(z)$ whereas the crosses are $\Theta(z)$. Parameters as on graph. The vertical dotted lines are where $\zeta = 0.329, \xi = 0.671$.

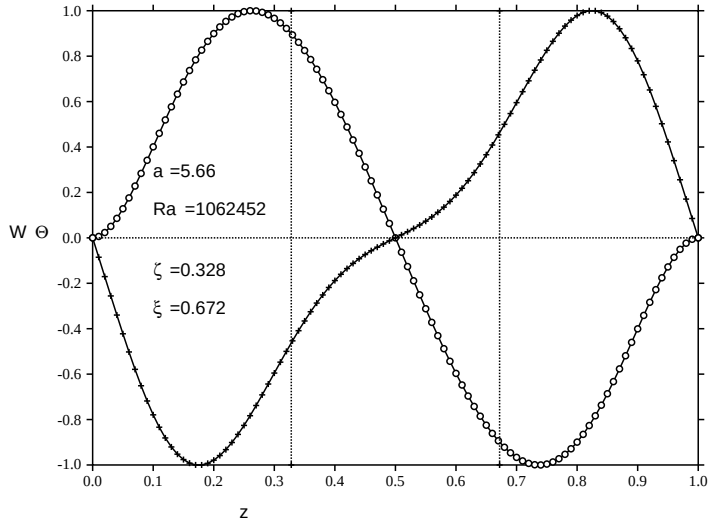

Figure 7: Linear instability eigenfunctions at criticality. The open circles represent $W(z)$ whereas the crosses are $\Theta(z)$. Parameters as on graph. The vertical dotted lines are where $\zeta = 0.328, \xi = 0.672$.

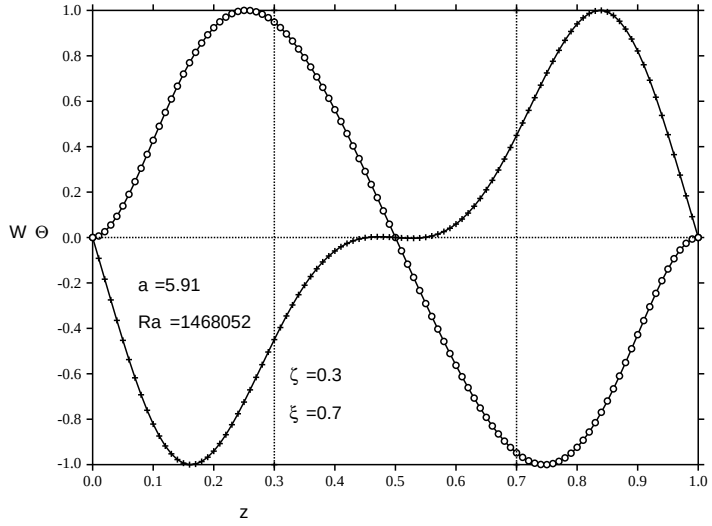

Figure 8: Linear instability eigenfunctions at criticality. The open circles represent $W(z)$ whereas the crosses are $\Theta(z)$. Parameters as on graph. The vertical dotted lines are where $\zeta = 0.3, \xi = 0.7$.

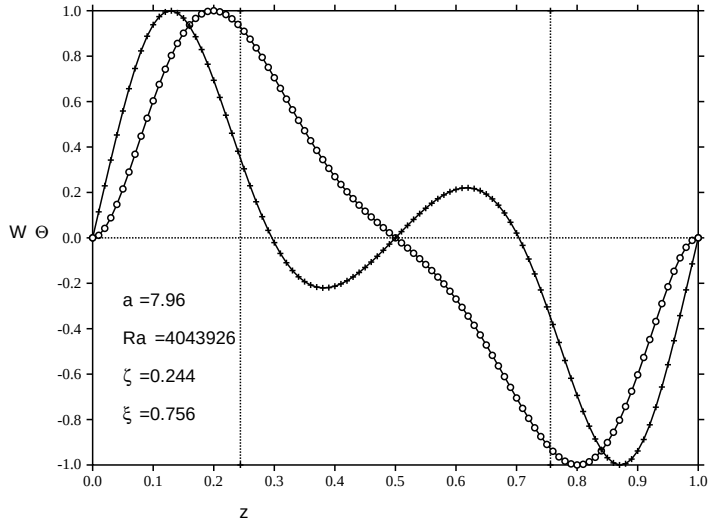

Figure 9: Linear instability eigenfunctions at criticality. The open circles represent $W(z)$ whereas the crosses are $\Theta(z)$. Parameters as on graph. The vertical dotted lines are where $\zeta = 0.244, \xi = 0.756$.

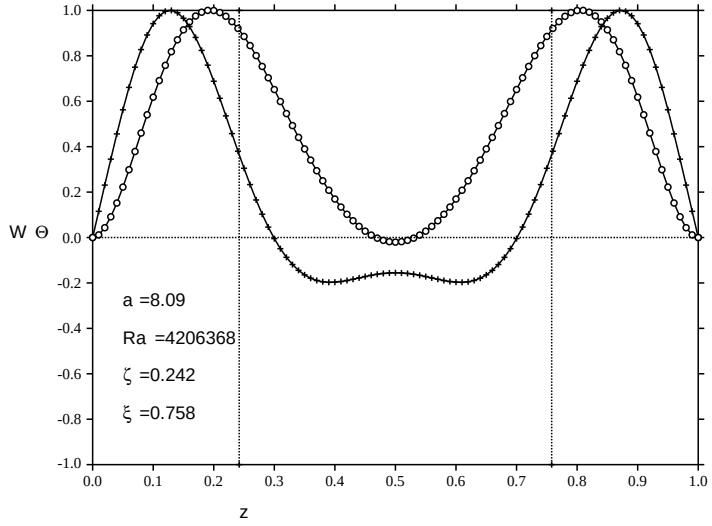

Figure 10: Linear instability eigenfunctions at criticality. The open circles represent $W(z)$ whereas the crosses are $\Theta(z)$. Parameters as on graph. The vertical dotted lines are where $\zeta = 0.242, \xi = 0.758$.

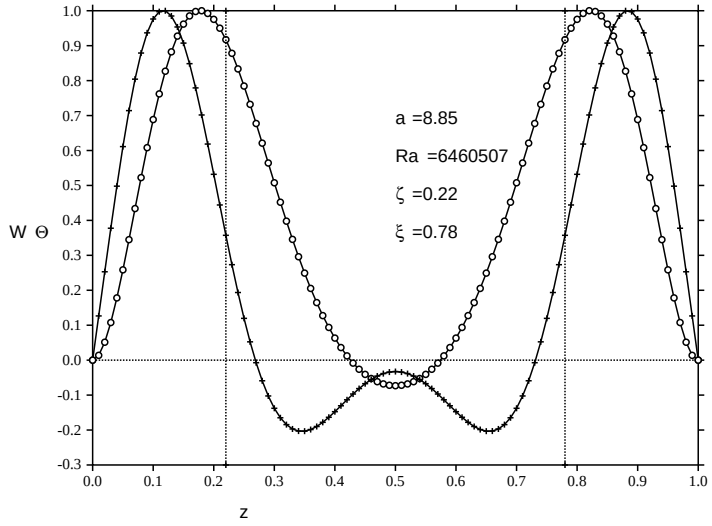

Figure 11: Linear instability eigenfunctions at criticality. The open circles represent $W(z)$ whereas the crosses are $\Theta(z)$. Parameters as on graph. The vertical dotted lines are where $\zeta = 0.22, \xi = 0.78$.

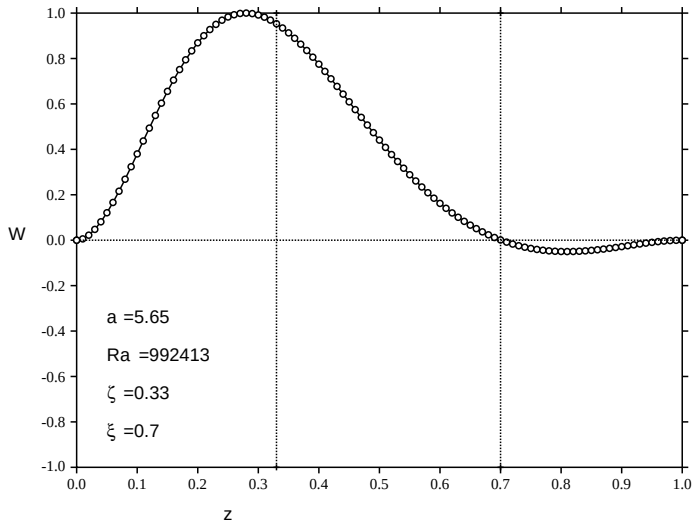

Figure 12: W eigenfunction at criticality, parameters as on figure; the vertical dotted lines are where $\zeta = 0.33, \xi = 0.7$.

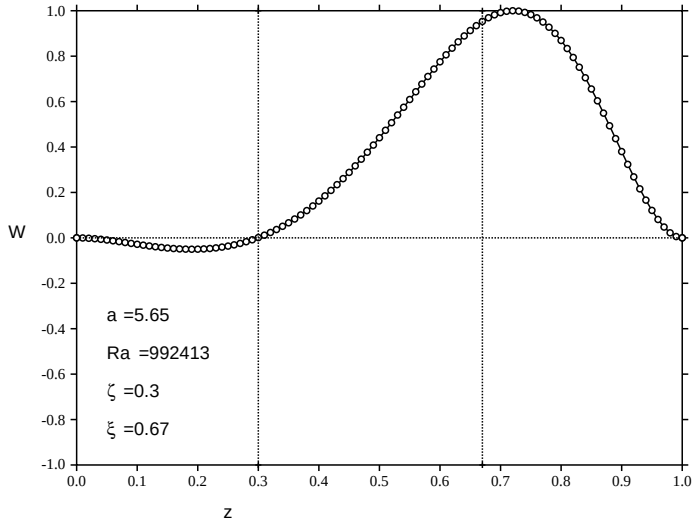

Figure 13: W eigenfunction at criticality, parameters as on figure; the vertical dotted lines are where $\zeta = 0.3, \xi = 0.67$.

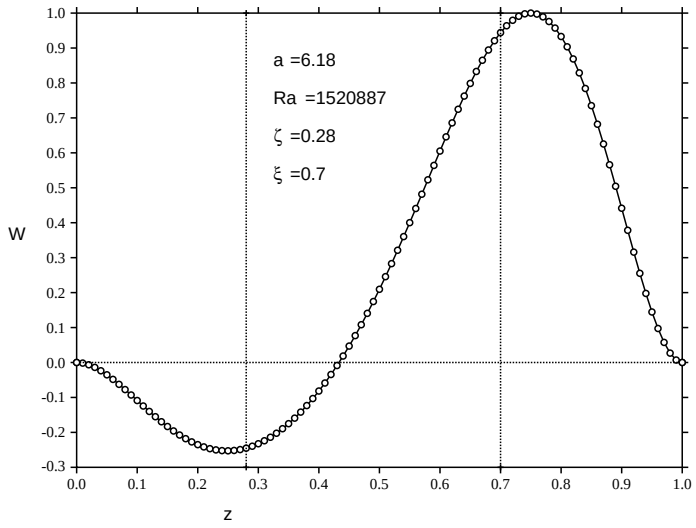

Figure 14: W eigenfunction at criticality, parameters as on figure; the vertical dotted lines are where $\zeta = 0.28, \xi = 0.7$.

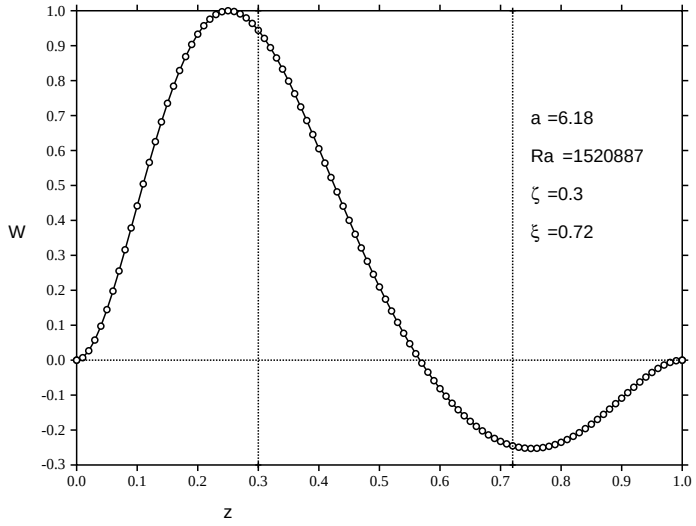

Figure 15: W eigenfunction at criticality, parameters as on figure; the vertical dotted lines are where $\zeta = 0.3, \xi = 0.72$.

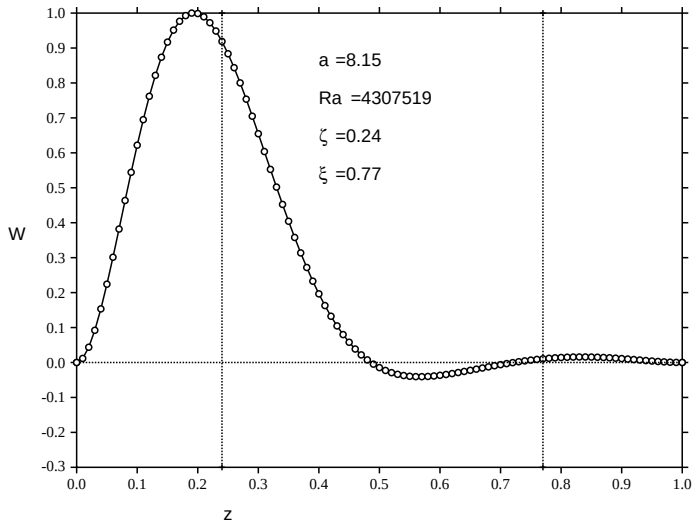

Figure 16: W eigenfunction at criticality, parameters as on figure; the vertical dotted lines are where $\zeta = 0.24, \xi = 0.77$.

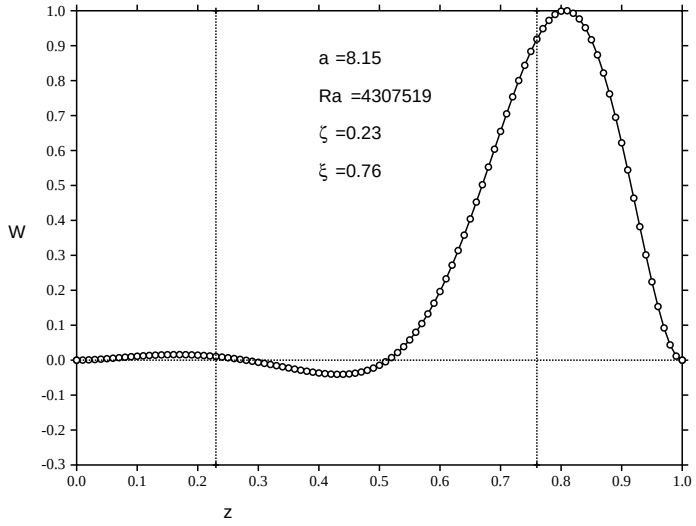

Figure 17: W eigenfunction at criticality, parameters as on figure; the vertical dotted lines are where $\zeta = 0.23, \xi = 0.76$.